Potentiating hypoxic microenvironment for antibiotic activation by photodynamic therapy to combat bacterial biofilm infections

Weijun Xiu

  Key Laboratory for Organic Electronics and Information Displays and Jiangsu Key Laboratory for Biosensors, Institute of Advanced Materials (IAM), Nanjing University of Posts and Telecommunications

Ling Wan

  Nanjing University of Posts and Telecommunications

Kaili Yang

  Key Laboratory for Organic Electronics and Information Displays and Jiangsu Key Laboratory for Biosensors, Institute of Advanced Materials (IAM), Nanjing University of Posts and Telecommunications

Xiao Li

  Key Laboratory for Organic Electronics and Information Displays and Jiangsu Key Laboratory for Biosensors, Institute of Advanced Materials (IAM), Nanjing University of Posts and Telecommunications

Lihui Yuwen

  Key Laboratory for Organic Electronics and Information Displays and Jiangsu Key Laboratory for Biosensors, Institute of Advanced Materials (IAM), Nanjing University of Posts and Telecommunications
  https://orcid.org/0000-0001-5313-9565

Heng Dong

  Nanjing University

Yongbin Mou

  Nanjing University

Dongliang Yang

  Nanjing Tech University

Lianhui Wang (✉ iamlhwang@njupt.edu.cn)

  Nanjing University of Posts and Telecommunications   https://orcid.org/0000-0001-9030-9172

Article

Version of Record: A version of this preprint was published at Nature Communications on July 5th, 2022. See the published version at https://doi.org/10.1038/s41467-022-31479-x.

Abstract

Traditional antibiotic treatment has limited efficacy for the drug-tolerant bacteria present in biofilms because of their unique metabolic conditions in the biofilm infection microenvironment. Modulating the biofilm infection microenvironment may influence the metabolic state of the bacteria and provide novel therapeutic routes. Here, photodynamic therapy (PDT)-activated chemotherapy by potentiating the hypoxia of biofilm infection microenvironment is proposed to tackle methicillin-resistant *Staphylococcus aureus* (MRSA) biofilm infections. In this study, PDT was used not only to eradicate MRSA biofilms in normoxic conditions, but also to potentiate the hypoxic microenvironment, which induces the anaerobic metabolism of MRSA and activates metronidazole to kill bacteria. Moreover, PDT-activated chemotherapy could polarize the macrophages to a M2-like phenotype and promote the repair of the biofilm infected wounds in mice. This biofilm infection microenvironment modulation strategy, whereby the hypoxic microenvironment is potentiated to synergize PDT with chemotherapy, provides an alternative pathway for efficient treatment of biofilm-associated infections.

Introduction

Bacterial biofilm-related infections affect millions of people worldwide and pose a serious threat to the public healthcare system [1, 2, 3, 4, 5]. In biofilms, bacteria are packed together by self-secreted extracellular polymeric substances (EPS) [6]. Shielded by such compact frameworks, bacteria can develop antibiotic tolerance because of their varied metabolic states to adapt to the biofilm infection microenvironment (BIM) [1, 7, 8, 9, 10, 11, 12]. On the other hand, bacteria in biofilms can avoid the immune attack under the protection of EPS. The infiltrating immune cells around bacterial biofilms produce excessive inflammatory factors, which causes the infected tissues to remain in the inflammatory phase and impede the normal healing process [13, 14, 15, 16]. Consequently, the bacterial biofilms are usually associated with recalcitrant infections and serious inflammation. Clinically, high-dose antibiotics and surgical resection are the primary choices to treat bacterial biofilm infections; however, they are frequently ineffective or too painful [17, 18]. Therefore, an effective therapeutic strategy for bacterial biofilm infections remains an urgent need.

Owing to the complicated interactions between the bacteria and host, the biofilm infected tissues usually have a unique microenvironment, such as low pH, hypoxia, specific enzymes, lack of nutrients, and so on [10, 19]. Importantly, the BIM greatly influences the metabolic activity state of bacteria and is closely related to the therapeutic outcome of antibiotics [20, 21]. To adapt to the complex BIM, bacteria in biofilms can develop diverse phenotypes with various metabolic states and drug susceptibility [10, 20, 21, 22]. Although antibiotics can kill most metabolically active bacteria in biofilms, metabolically less active bacteria that are deeply located in biofilms have high antibiotic tolerance, which causes incomplete bacteria-killing and the relapse of biofilm infections [7, 10, 12, 23]. Hence, the BIM has a close relationship with the efficiency of antibiotics, and the modulation of the BIM may provide new opportunities for managing bacterial biofilm infections.

Herein, we develop the hypoxia-potentiating strategy by combining the PDT and the prodrug MNZ to treat bacterial biofilm infections. As shown in Fig. 1a, HA-Ce6-MNZ nanoparticles (HCM NPs) were prepared by functionalizing hyaluronic acid (HA) with Chlorin e6 (Ce6) and MNZ. Following delivery into MRSA biofilm infected sites, HCM NPs are decomposed to release Ce6 and MNZ by hyaluronidase (Hyal) secreted from MRSA. During laser irradiation, Ce6 could generate $^1O_2$ and kill the bacteria in biofilms under normoxic conditions. The depletion of O_2 by PDT subsequently potentiates hypoxia in biofilms and promotes the generation of nitroreductase by MRSA, which could further reductively activate MNZ and kill the metabolically less active bacteria under hypoxic conditions. Such PDT-activated chemotherapy can be used to eradicate MRSA biofilms, and macrophages in infected tissues can be further polarized to a M2-like phenotype to facilitate tissue healing (Fig. 1b). The superior therapeutic efficacy of HCM NPs was studied in subcutaneous MRSA biofilm infected mice. Moreover, *in situ* sprayed fibrin gel containing HCM NPs was demonstrated to be effective in treating MRSA biofilm infected chronic wounds in diabetic mice. This work highlights a BIM-modulation strategy to efficiently combat bacterial biofilm-related infections.

Results

Preparation and characterization of HCM NPs.

In this study, HA-Ce6 was synthesized by conjugating Ce6 to amine-functionalized HA (A-HA), which can self-assemble into HA-Ce6 NPs (HC NPs) [24]. Then, MNZ was loaded into HC NPs to form HCM NPs (Fig. 2a). As shown in Fig. 2b-d, HCM NPs have a spheroid morphology similar to HC NPs, and an increased hydrodynamic diameter. The zeta potential results show that both HC NPs and HCM NPs have negative charges (Fig. 2e), indicating the successful functionalization of A-HA. As shown in Fig. 2f and Supplementary Fig. 1, the IR absorption bands at 1485 cm^{-1} and 1716 cm^{-1} can be assigned to the stretching vibration of N=O (-NO$_2$) from MNZ and the bending vibration of C=O from Ce6, respectively [25, 26]. Besides, the characteristic peaks near 400 nm and 660 nm for Ce6, and 320 nm for MNZ emerged in the absorption spectrum of HCM NPs, demonstrating the successful preparation of HCM NPs (Fig. 2g).

As MRSA can secrete Hyal and decompose HA [3], Hyal in MRSA biofilms can be used to trigger the drug release of HCM NPs (Fig. 3a). First, the Hyal-responsive release of Ce6 and MNZ was studied. In HCM NPs, the fluorescence of Ce6 was quenched because of its aggregated form (Supplementary Fig. 2) [27]. Fig. 3b and c, indicate that the fluorescence of HCM NPs recovered with the presence of Hyal under acidic conditions (pH 5.5). The release efficiency of Ce6 and MNZ from HCM NPs was approximately 80% and 78%, respectively, after 24 h incubation with Hyal (Fig. 3d and e). As illustrated in Fig. 3f and g, the fluorescence signal of Ce6 showed significant recovery after the incubation of HCM NPs with MRSA biofilms, while that of HCM NPs incubated with mammalian cells (mice smooth muscle cells, SMCs) showed a neglectable increase. After incubating for 24 h, the fluorescence signal of Ce6 in MRSA biofilms was approximately 2-fold higher than that incubated with SMCs (Supplementary Fig. 3), indicating that HCM NPs can effectively release the loaded drugs in MRSA biofilms. Hyal induced decomposition of HCM NPs was also confirmed by DLS and TEM (Fig. 3h and i). Besides, the $^1O_2$ generation property of

HCM NPs under light irradiation was measured by using 9, 10-anthracenediyl-bis(methylene)-dimalonic acid (ABDA) as an indicator [28]. As shown in Fig. 3j, the $^1O_2$ generation of HCM NPs in the presence of Hyal was higher than that of other groups, indicating their Hyal-responsive photodynamic effect.

Before further biomedical application study, the colloidal stability and cytotoxicity of HCM NPs were evaluated. HCM NPs showed no obvious aggregation and change of diameter after dispersing in different mediums (H_2O, phosphate buffered saline (PBS), and minimum Eagle's medium (MEM)) for 24 h, indicating good colloidal stability (Supplementary Fig. 4). As shown in Supplementary Fig. 5, the viability of human normal liver (L-O2) cells exceeded 90% after being incubated with HCM NPs (Ce6: 160 μg/mL) for 1 d. In contrast, the viability of L-O2 cells decreased below 65% after incubation with HCM NPs (Ce6: 160 μg/mL) in the medium containing Hyal.

Enhanced in vitro anti-biofilm effect of HCM NPs by potentiating hypoxia.

As a facultative anaerobe, *S. aureus* can grow using either aerobic respiration in normoxic conditions or using nitrate and mixed fermentation under hypoxic conditions [29, 30]. In biofilms, bacteria exhibit various metabolic states owing to the complex BIM, which has significant implications for the therapeutic efficiency of antibiotics. Although the facultative bacteria in biofilms with normoxic conditions can be effectively inactivated by antibiotics, the bacteria in biofilms under hypoxic conditions usually show significant drug tolerance due to their anaerobic metabolic state [31]. As a prodrug, MNZ could be activated with the assistance of electron transfer proteins, such as nitroreductase, in the cytoplasm of bacteria under low redox potential [32, 33, 34]. Amine derivatives reduced from MNZ can induce the damage of DNA helix and cause bacterial death. Although MNZ is commonly used to treat anaerobe infections, it has also been reported with limited effect for facultative anaerobes [35, 36, 37]. In the hypoxic BIM, MRSA can overexpress nitroreductase (Supplementary Fig. 6), which may activate the antibacterial activity of MNZ for killing facultative anaerobe [38, 39]. As shown in Supplementary Fig. 7, the viability of MRSA showed a neglectable decrease following treatment with MNZ (100 μg/mL) under normoxic conditions, while approximately 25% of MRSA were killed by MNZ under hypoxic conditions. The combination of MNZ with oxygen-consuming PDT could work synergistically; therefore, we hypothesized that PDT could inactivate the bacteria under normoxic conditions, deplete O_2 in the local environment, potentiate the hypoxic condition within biofilms, promote the expression of nitroreductase by bacteria, and finally activate MNZ to kill the remaining bacteria inside biofilms (Fig. 4a).

To prove the above hypothesis, the anti-biofilm effect of HCM NPs was evaluated by MRSA biofilms *in vitro*. As shown in Fig. 4b, MRSA biofilms showed significantly decreased the level of O_2 following the treatment of HCM NPs with laser irradiation, indicating that PDT could potentiate the hypoxia level of biofilms. As indicated in Fig. 4c and d, the MRSA inactivation efficiency for HC NPs with laser irradiation (3.1 log, 99.92%) was much higher than that of vancomycin (Van, 0.7 log, 78.3%) or MNZ (0.2 log, 12.3%). In contrast, HCM NPs with laser irradiation can inactivate MRSA by 5.9 log (99.9998%), much higher than PDT or antibiotic treatment alone, which demonstrates the superiority of PDT-activated chemotherapy.

Besides, the MRSA biofilms showed significant structural damage and decreased biofilm biomass after treatment of HCM NPs with laser irradiation (Fig. 4e and f). The SEM images further indicate the excellent therapeutic efficacy of HCM NPs (Fig. 4g).

The long-term anti-biofilm effect was studied to evaluate the therapeutic effectiveness of PDT-activated chemotherapy. From Supplementary Fig. 8a and b, the live bacteria in MRSA biofilms treated by HCM NPs with laser irradiation (HCM+L) showed no significant increase at 72 h post-treatment under eutrophic conditions, while the bacteria in other groups showed obvious regrowth. Moreover, the micrographs of MRSA biofilms stained by crystal violet in the HCM+L group show that the biofilm structure was completely destructed without regrowth in 3 d after treatment (Supplementary Fig. 8c), which was not achieved by other treatments. Therefore, PDT-activated chemotherapy could completely eradicate MRSA biofilms and prevent their regrowth.

Treatment of subcutaneous MRSA biofilm infected mice.

To evaluate the *in vivo* anti-biofilm efficacy of HCM NPs, the subcutaneous MRSA biofilm infected mice model was constructed (Fig. 5a) [40]. As shown in Fig. 5b, the fluorescence signal appeared in MRSA biofilm infected sites after *in situ* injection of HCM NPs, while a limited fluorescence signal was observed for normal tissues. HCM NPs were also intravenously (*i.v.*) injected into MRSA biofilm infected mice. The fluorescence signal from Ce6 was obviously increased in MRSA biofilm infected tissues and peaked at 12 h post-injection (Fig. 5c and d). Meanwhile, the fluorescence images of the biofilm infected tissue and major organs harvested from mice also demonstrate similar results, suggesting efficient accumulation and drug release of HCM NPs in biofilm infected tissues (Supplementary Fig. 9) [19, 41].

The hypoxia level of infected tissues after various treatments was further evaluated by using immunofluorescence staining of hypoxia inducible factor-1α (HIF-1α). As shown in Fig. 5e-g, the overexpression of HIF-1α and vascular endothelial growth factor (VEGF) in HC+L and HCM+L groups indicates that PDT could potentiate the hypoxia level in biofilm infected tissues. As shown in Fig. 5h and i, the infected tissue almost disappeared at 8 d post-treatment in the HCM+L group, while that in other groups showed a limited reduction. Moreover, the bacterial inactivation efficiency was approximately 6.4 log (99.99996%) in the HCM+L group, which was much better than that in other groups (Fig. 5j and k). These results indicate the excellent *in vivo* anti-biofilm efficacy of PDT-activated chemotherapy. As shown in Fig. 5l, the infected tissues of mice in HCM+L group exhibited little inflammatory cell infiltration and high extent of collagen deposition, while other groups still showed significant inflammation. Besides, the body weight and major organs of the mice in HCM+L group showed no observable abnormalities, indicating low toxicity of HCM NPs (Supplementary Fig. 10).

Macrophage polarization after PDT-activated chemotherapy.

For biofilm-related infections, the long-term existence of bacteria causes a persistent inflammatory state in the infected tissues, and seriously disturbs the normal repair process [13]. Macrophages perform critical regulatory functions in different tissue repair stages by polarization [42, 43, 44]. M1-like macrophages

associate with inflammation of the infected tissues, while M2-like macrophages have key roles in tissue repair [42, 45]. Hence, the influence of PDT-activated chemotherapy on macrophage polarization in tissues was further evaluated. As shown in Fig. 6a-c, the infected tissues of mice in HCM+L groups showed decreased M1-like macrophages (F4/80$^+$ and CD80$^+$) infiltration and increased M2-like macrophages (F4/80$^+$ and CD206$^+$) infiltration compared with the other groups. Furthermore, the lower level of interleukin-12p70 (IL-12p70) and higher level of interleukin-4 (IL-4) in HCM+L group than in other groups suggest that the macrophages are polarized to M2 phenotype after PDT-activated chemotherapy (Fig. 6d and e). This macrophage polarization was further confirmed by the high expression of CD206 and the low expression of CD80 in infected tissues in HCM+L group (Fig. 6f and g). The increase of tumor necrosis factor-α (TNF-α), IL-12p70, and IL-6, and the decrease of transforming growth factor-β (TGF-β), IL-4, and Arginase-1 (Arg-1) also suggest the M2 polarization in HCM+L group (Fig. 6h and i). Therefore, PDT-activated chemotherapy could be used to polarize macrophages to an anti-inflammatory phenotype and promote the tissue healing.

Treatment of MRSA biofilm infected wounds in diabetic mice.

Nowadays, up to 25% of patients with diabetics confront a lifetime risk of chronic wounds, which may lead the amputation and even death [46]. One of the major reasons for the therapeutic failure of diabetic chronic wounds is the formation of bacterial biofilms, which often develop superimposed infections and delay the repair process [47]. Here, we prepared HCM NPs-based fibrin gel (HCM gel) to treat MRSA biofilm infected wounds in diabetic mice. As shown in Fig. 7a, the HCM gel was formed *in situ* after sequentially spraying HCM NPs-containing fibrinogen solution and thrombin solution on the wound bed (Fig. 7b). CLSM images of the HCM gel demonstrate that the distribution of the fluorescence signal from Ce6 is consistent with that from fibrin, suggesting the successful encapsulation of HCM NPs in the fibrin gel (Fig. 7c).

To evaluate the *in vitro* drug release capability, HCM gels were incubated with or without Hyal (200 unit/mL) under different pH conditions. As illustrated in Fig. 7d and e, Ce6 and MNZ were gradually released under acidic conditions in presence of Hyal. After *in situ* formation of the HCM gel, the fluorescence signal gradually increased in MRSA biofilm infected wounds, while the fluorescence signal of the normal wounds was relatively unchanged (Fig. 7f and g), indicating that the HCM gel can release the loading drugs in the BIM. Then, the anti-biofilm efficacy of the HCM gel by PDT-activated chemotherapy was evaluated in diabetic mice (Fig. 8a). Following 12 d of treatment, the infected wounds in HCM+L group completely disappeared, while those in other groups still remained unhealed (Fig. 8b and c). Notably, the HCM+L group displayed the best bacterial inactivation efficiency (8.0 log, 99.999999%), which is much higher than that shown by HC group (4.3 log, 99.994%), HCM group (4.9 log, 99.999%), and HC+L group (6.7 log, 99.99997%) (Fig. 8d and Supplementary Fig. 11).

The overexpression of HIF-1α in HCM+L group indicates that PDT could exacerbate hypoxia level of the biofilm infected tissues (Supplementary Fig. 12). The immunofluorescence images reveal that the M1-like macrophages decreased and the M2-like macrophages increased in HCM+L group (Fig. 8e-g), suggestive

of macrophage polarization to the M2-like phenotype in infected wounds. The decreased secretion of TNF-α and IL-12p70, and the increased secretion of Arg-1 and IL-4 in HCM+L group further confirm the M2-like macrophage polarization (Fig. 8h-k). H&E and Masson's trichrome staining photographs show significant re-epithelialization, collagen deposition, and less inflammatory cell infiltration in the biofilm infected tissues from HCM+L group, demonstrating the superior therapeutic efficacy of PDT-activated chemotherapy (Fig. 8l). After being treated by the HCM gel with laser irradiation, the mice showed no decrease in body weight and no obvious inflammation in major organs (Supplementary Fig. 13).

Discussion

Traditional antibiotic treatment is generally insufficient to completely eliminate the existed bacterial biofilms [2, 11, 12]. In contrast to bacteria in planktonic form, bacteria in biofilms possess heterogeneous physiological activity to adapt to the complex BIM, which greatly reduces the therapeutic effect of antibiotics. For instance, the bacteria in the out layer of biofilms have an active metabolic state with high susceptibility to antibiotics, while the bacteria that are located deep within biofilms exhibit reduced metabolic activity and low susceptibility to antibiotics due to the limited oxygen and nutrients [2, 10, 19, 48]. Besides, the bacteria in biofilms can escape the host immune attack due to the protection of EPS, which continuously induces inflammatory response and seriously impedes the tissue repair process [12, 13, 23, 47]. Therefore, it is essential to completely eliminate bacteria in biofilms and mitigate the inflammation for effective treatment of biofilm infections.

Compared to antibiotic treatment, PDT can efficiently kill various bacteria by generating $^1O_2$ [3, 40]. However, the hypoxic condition of biofilms significantly restricts the efficiency of PDT. On the other side, MNZ has been widely used for the patients with anaerobic bacterial infections. As a prodrug, MNZ could be reductively activated under low oxygen levels by forming imidazole fragments with high cytotoxicity toward anaerobic bacteria. Nevertheless, MNZ has been reported to have neglectable efficacy for use in infections with facultative anaerobes [35, 37]. As facultative anaerobes in hypoxic conditions can secrete electron transfer proteins, such as nitroreductase, which may transform MNZ to cytotoxic fragmentation [35, 36, 37], we hypothesized that MNZ could be activated under hypoxia caused by PDT to kill facultative anaerobes. In this study, HCM NPs were developed as novel therapeutic nanoagents to treat MRSA biofilm infections by hypoxia-potentiation. During laser irradiation, Ce6 generates $^1O_2$ and kills the MRSA in biofilms via the consumption of O_2, which subsequently induces the hypoxic condition. MRSA in hypoxic BIM alter their metabolic state and generate electron transfer proteins for MNZ activation. The activated MNZ can further kill the bacteria in metabolically less active state within biofilms, which could not be achieved by antibiotic treatment or PDT alone. In biofilm infected mice, bacteria inside biofilm infected tissues were efficiently eliminated by PDT-activated chemotherapy in both subcutaneous biofilm infected mice (5.9 log) and biofilm infected wounds in diabetic mice (8.0 log), indicating the effectiveness of the hypoxia potentiation strategy.

In biofilm infected tissues, macrophages play important regulatory roles in all stages of tissue repair [49]. Although the immediate inflammatory response is essential for bacterial inactivation, the existence of bacterial biofilms usually causes persistent inflammation, which seriously retards tissue healing [10, 12, 13]. The polarization of macrophages into anti-inflammatory (M2) phenotype is desired for the healing of biofilm infected tissues [13, 44, 49]. In this work, M2-like macrophages were significantly increased in infected tissues after PDT-activated chemotherapy, which can greatly facilitate the inflammation inhibition and tissue healing.

Effective treatment of biofilm related infections remains a great challenge owing to the drug-tolerant bacteria in biofilms. Although PDT-activated chemotherapy has shown promising results both *in vitro* and *in vivo*, the poor penetration depth of the visible light limits its further application for deep tissue infections [3]. Thus, PDT-activated chemotherapy may be used for superficial tissue infections, such as diabetic foot. The combination of MNZ with other oxygen dependent therapies with deep tissue penetration, such as sonodynamic therapy, may overcome this issue.

The PDT-activated chemotherapy can efficiently treat bacterial biofilm infections and promote tissue healing by facilitating macrophage polarization toward the M2-like phenotype. Hence, this work establishes a promising strategy to deal biofilm-related infections based on hypoxia potentiation, and sheds light on the rational design of novel therapeutic nanoagents for effective management of the bacterial biofilm-related infections.

Methods

Materials. Metronidazole, vancomycin (Van), 1-(3-dimethylaminopropyl)-3-ethylcarbodiimide hydrochloride (EDC), N-hydroxysulfosuccinimide sodium salt (sulfo-NHS), hyaluronidase (Hyal), fibrinogen, thrombin, dimethyl sulfoxide (DMSO), dimethylformamide (DMF), 9, 10-anthracenediyl-bis(methylene)-dimalonic acid (ABDA), and ethylenediamine were obtained from Sigma-Aldrich; sodium hyaluronate (200 kDa) was purchased from SunlidaBio; and Ce6 was bought from JenKem Technology.

Preparation of HA-Ce6-MNZ nanoparticles (HCM NPs). Firstly, EDC (16.7 mg), sulfo-NHS (12.1 mg), and sodium hyaluronate (0.2 g) were dissolved in phosphate buffer saline (PBS, 10 mM, pH 7.4, 10 mL) and stirred for 30 min. Then, ethylenediamine (0.2 g, dispersed in PBS) was mixed with the above solution for 12 h at room temperature (RT), dialyzed against PBS for 2 d, and further freeze-dried to obtain A-HA. EDC (1.6 mg), sulfo-NHS (1.3 mg), and Ce6 (20 mg) were dissolved in DMSO solution (10 mL) and stirred for 30 min, followed by adding 10 mL A-HA solution (DMF: H_2O = 1:1, 4 mg/mL) and reacting for 12 h at RT. The reaction mixture was diluted with 40 mL PBS, ultrasonicated for 15 min, and dialyzed against PBS for 2 d to form HC NPs. Subsequently, 10 mg freeze-dried HC NPs were dissolved in 10 mL DMSO-H_2O solution (1:1) and mixed with MNZ (100 mg) for 12 h at RT, then dialyzed against PBS for 2 d to obtain HCM NPs.

Preparation of HCM gel. To form the HCM gel, PBS buffers containing HCM NPs (Ce6: 200 µg/mL, MNZ: 100 µg/mL) and fibrinogen (10 mg/mL) were mixed as solution A. Thrombin solution (10 NIH U/mL) in $CaCl_2$ (0.1 M) was used as solution B. After spraying solution A and solution B at an equal volume by using a dual-cartridge sprayer, the HCM gel were formed in several minutes.

Hyal-responsive drug release of HCM NPs. HCM NPs (Ce6: 40 µg/mL; MNZ: 20 µg/mL) were dispersed in PBS with different pH values (7.4 and 5.5) with or without Hyal (200 unit/mL) and gently shaken at 37°C. The Ce6 and MNZ released from HCM NPs were separated from the mixtures by ultrafiltration. The released Ce6 and MNZ were quantified by using UV-Vis absorption spectroscopy.

Detection of singlet oxygen. The ABDA was used for detecting $^1O_2$. Briefly, different agents and ABDA (10 µg/mL) were dissolved in PBS and exposed with 635 nm laser (20 mW/cm^2) for different times. The $^1O_2$ can react with ABDA, which can be monitored via the decrease in absorbance at 380 nm.

Cell culture. Human normal liver (L-O2) cells and mouse smooth muscle cells (SMCs) were purchased from KeyGen BioTech. These cells were cultured in Dulbecco's modified eagle medium (DMEM) containing 10% fetal bovine serum (FBS, Gibco) at 37°C under 5% CO_2.

Bacterial culture. Methicillin-resistant *Staphylococcus aureus* (MRSA, ATCC43300) were grown in chemically defined medium [50], and then incubated in Luria-Bertani (LB) medium (containing 1% glucose, 10^7 CFU/mL) at 37°C for 2 d to form MRSA biofilms.

Cytotoxicity of HCM NPs. L-O2 cells were grown in 96-well plates with 10^4 cells per well for 1 d. Then, L-O2 cells were incubated with HCM NPs dispersions with different concentrations for 1 d. Cell viability was determined by using LDH Cytotoxicity Colorimetric Assay Kit (BioVision).

Evaluation of the nitroreductase activity of MRSA. The activity of nitroreductase from MRSA in biofilms was analyzed according to the previous work [36]. Briefly, MRSA biofilms were incubated under hypoxic (5% O_2) or normoxic conditions for 48 h. The MRSA were collected, washed three times with Tris-HCl buffer (20 mM, pH 7.6) at 4°C, incubated with lysostaphin (50 µg/mL) and deoxyribonuclease I (DNase I, 50 µg/mL) for 30 min at 37°C, respectively, and centrifuged (13000 × g) for 0.5 h at 4°C. The nitroreductase activity in cell extracts was determined by using nitrofurantoin (50 µM) and nitrofurazone (50 µM) as substrates, and nicotinamide adenine dinucleotide phosphate (NADPH, 250 µM) or nicotinamide adenine dinucleotide (NADH, 250 µM) as electron donors. The absorbance at 400 nm for nitrofurazone and absorbance at 420 nm for nitrofurantoin was measured by using a microplate reader (PowerWave XS2, BioTek) to evaluate the nitroreductase activity.

In vitro anti-biofilm effect. Preformed MRSA biofilms were incubated with the saline solutions of MNZ (25 µg/mL), Van (50 µg/mL), HC (Ce6: 50 µg/mL), and HCM (Ce6: 50 µg/mL, MNZ: 25 µg/mL) for 6 h, respectively. The Calcein-AM was used to stain the viable bacteria inside MRSA biofilms after various treatments. To observe the structure of biofilm, MRSA biofilms were fixed with formalin for 10 min and

washed with saline for three times. After natural drying, the fixed MRSA biofilms were stained with crystal violet solution (0.02%) for 0.5 h, and imaged on a fluorescence microscope (Olympus IX71). To calculate the colony numbers of MRSA in biofilms, the samples were sonicated in saline for 5 min and tested by plate counting method. To study the long-term inhibition by HCM NPs, MRSA biofilms were treated by Van (50 µg/mL), HC NPs (Ce6: 50 µg/mL), and HCM NPs (Ce6: 50 µg/mL, MNZ: 25 µg/mL) dispersed in chemically defined medium with or without laser irradiation, and further incubated for 72 h to evaluate the anti-biofilm efficacy by using the crystal violet staining method.

SEM imaging of MRSA biofilms. Following various treatments, MRSA biofilms were fixed by 2.5% glutaraldehyde solution for 30 min. Then, the samples were dehydrated by graded ethanol solutions (15%, 30%, 50%, 75%, and 100%) for 15 min, respectively. The samples were sputter-coated with gold and imaged by using a scanning electron microscope (Hitachi S4800).

Assessment of the hypoxia level of MRSA biofilms. MRSA biofilms were growth on Petri dishes and incubated with HCM NPs in chemically defined medium (Ce6: 50 µg/mL, MNZ: 25 µg/mL) for 6 h. After 635 nm laser irradiation (20 mW/cm^2, 30 min), MRSA biofilms were stained with $[Ru(dpp)_3]Cl_2$ (10 µg/mL) for 6 h. Fluorescence images of MRSA biofilms were obtained using a confocal laser scanning microscope (Olympus IX81).

In vivo fluorescence imaging of biofilm infections. Female Balb/c mice (20 g, 6-8 weeks old) were purchased from Nanjing Junke Biological Engineering Co., Ltd. All animal procedures were performed in accordance with the Guidelines for the Care and Use of Laboratory Animals of Nanjing Tech University and approved by the Animal Ethics Committee of Nanjing Tech University. LB medium dispersions of MRSA (10^9 CFU/mL, with 1% glucose) were subcutaneously injected into the right thigh of mice and infected for 48 h to form subcutaneous biofilm infections. Fluorescence images of mice were captured on a IVIS Lumina K Series III system (Perkin Elmer) post *i.v.* injection of HCM NPs (Ce6 = 4 mg/kg; MNZ = 2 mg/kg) at given time points.

Treatment of subcutaneous biofilm infected mice by HCM NPs. MRSA biofilm infected mice were *i.v.* injected with HCM NPs (Ce6 = 4 mg/kg; MNZ = 2 mg/kg) and irradiated with 635 nm laser (20 mW/cm^2, 30 min) at 8th h post-injection. The area of infected tissue was calculated as follows: area = (width/2 × length/2) × π. The infected tissues from mice were captured following an 8 d treatment period, and the bacteria were separated by ultrasonication for 15 min. The number of bacteria in the infected tissues was measured by the plate counting method. For histological analysis, all samples were fixed with 10% formalin, embedded in paraffin, and sliced for H&E and Masson's trichrome staining.

Treatment of biofilm infected wounds in diabetic mice by HCM gel. Male C57BL/6 mice were intraperitoneal (*i.p.*) injected with streptozotocin (STZ) (60 mg/kg) every 3 days for 2 weeks. Blood glucose levels > 16.7 mM indicated the establishment of diabetic mice [51]. A circular cut (8 mm in diameter) was excised in the backs of diabetic mice, incubated with MRSA biofilm dispersions (10^7 CFU), and dressed with semiocclusive transparent films (Tegaderm, 3M) for 24 h to form MRSA biofilm infected

wounds. Then, the mixtures of different materials with fibrinogen and thrombin were sprayed on the wounds (Ce6 = 1 mg/kg; MNZ = 0.5 mg/kg) to form HCM gel. The wounds were irradiated with 635 nm laser (20 mW/cm^2, 30 min) at 12 h post-incubation. The infected tissues were harvested from mice at 12 d post-treatment and processed for histological analysis.

Immunofluorescence imaging. After various treatments for 4 d, the biofilm infected tissues were harvested from mice, fixed in 10% formalin, and then embedded in paraffin. After slicing, the tissue sections were incubated with 3% methanol for 10 min and 1% BSA for 20 min. The sections were then incubated with the primary antibodies, including anti-HIF-1α (Abcam, ab16066), anti-VEGF (Abcam, ab52917), anti-F4/80 (Abcam, ab6640), anti-CD80 (Abcam, ab254579), and anti-CD 206 (Abcam, ab64693), at room temperature for 2 h. Following incubation, the sections were incubated with fluorescently labeled secondary antibodies, including Alexa Fluor594-IgG (Abcam, ab150160), FITC-IgG (Jackson ImmunoResearch, 111-095-003), and tetramethylrhodamine (TRITC)-IgG (Jackson ImmunoResearch, 115-025-062) for 1 h. After further staining with 4',6-diamidino-2-phenylindole (DAPI), all slices were imaged by using a digital pathological section scanner (Olympus VS200).

Cytokine detection. The infected tissues and serums of mice were harvested at 4th d post-treatment. The cytokine level in tissues and serums was measured by ELISA kits (IL-6 (Abcam, ab222503), IL-4 (Abcam, ab100710), Arg-1 (Abcam, ab269541), TGF-β (Abcam, ab119557), TNF-α (Abcam, ab208348), and IL-12p70 (Abcam, ab119531)) according to the manufacturer's instructions.

Western blotting. The proteins were isolated from biofilm infected tissues at 4th d post-treatment. The content of protein was determined by using bicinchoninic acid protein assay (KeyGen BioTech). The gel electrophoresis and protein transformation were conducted by using western blotting kit (KeyGen BioTech) and the primary antibodies: anti-CD80 (Abcam, ab254579), and anti-CD 206 (Abcam, ab64693). The photographs were captured by G:BOX chemi-XR5 (Syngene) and relatively protein expression was quantified by using Gel-Pro Analyzer software.

Statistical analysis. All data were expressed as mean ± standard deviation (SD). Inter-group and intra-group comparison analyses in each experiment were calculated by unpaired Student's *t*-test analysis. Probability (*p*) values < 0.05 were considered statistically significant.

Data availability

All other data are available from the corresponding author upon reasonable request. Source data are provided with this paper.

Declarations

Acknowledgements

Author contributions

W.X., L.Y., and L. W. conceived the concept of the study and designed the experiments. W.X. performed the experiments and X.L. helped for the material characterizations. W.X., L.W., D.Y, and K.Y. performed the *in vitro* and *in vivo* experiments. H.D. and Y.M. helped and gave valuable suggestions for the *in vivo* experiments. W.X., L.Y., and L.W. analyzed the experimental data and co-wrote the manuscript. All the authors discussed, commented and agreed on the paper.

Competing interests

The authors declare no competing interests.

References

1. Costerton, J. W., Stewart, P. S. & Greenberg, E. P. Bacterial biofilms: A common cause of persistent infections. *Science* **284**, 1318–1322 (1999).

2. Flemming, H. C. et al. Biofilms: An emergent form of bacterial life. *Nat. Rev. Microbiol.* **14**, 563–575 (2016).

3. Xiu, W. et al. Recent development of nanomedicine for the treatment of bacterial biofilm infections. *VIEW* **2**, 20200065 (2021).

4. Burgener, E. B. et al. Filamentous bacteriophages are associated with chronic *Pseudomonas* lung infections and antibiotic resistance in cystic fibrosis. *Sci. Transl. Med.* **11**, eaau9748 (2019).

5. Lv, X. et al. Recent advances in pH-responsive nanomaterials for anti-infective therapy. *J. Mat. Chem. B* **8**, 10700–10711 (2020).

6. Hall-Stoodley, L., Costerton, J. W. & Stoodley, P. Bacterial biofilms: From the natural environment to infectious diseases. *Nat. Rev. Microbiol.* **2**, 95–108 (2004).

7. Olsen, I. Biofilm-specific antibiotic tolerance and resistance. *Eur. J. Clin Microbiol. Infect. Dis.* **34**, 877–886 (2015).

8. Lewis, K. Persister cells. *Annu. Rev. Microbiol.* **64**, 357–372 (2010).

9. Cohen, N. R., Lobritz, M. A. & Collins, J. J. Microbial persistence and the road to drug resistance. *Cell Host Microbe* **13**, 632–642 (2013).

10. Stewart, P. S. & Franklin, M. J. Physiological heterogeneity in biofilms. *Nat. Rev. Microbiol.* **6**, 199–210 (2008).

11. Penesyan, A., Gillings, M. & Paulsen, I. T. Antibiotic discovery: Combatting bacterial resistance in cells and in biofilm communities. *Molecules* **20**, 5286–5298 (2015).

12. Lewis, K. Persister cells, dormancy and infectious disease. *Nat. Rev. Microbiol.* **5**, 48–56 (2007).

13. Chen, C. et al. Ångstrom-scale silver particle–embedded carbomer gel promotes wound healing by inhibiting bacterial colonization and inflammation. *Sci. Adv.* **6**, eaba0942 (2020).

14. Chin, J., Madden, L., Chew, S. & Becker, D. L. Drug therapies and delivery mechanisms to treat perturbed skin wound healing. *Adv. Drug Delivery Rev.* **149-150**, 2–18 (2019).

15. Jensen, P., Kolpen, M., Kragh, K. & Kuhl, M. Microenvironmental characteristics and physiology of biofilms in chronic infections of CF patients are strongly affected by the host immune response. *APMIS* **125**, 276–288 (2017).

16. Kim, M. Nanoparticle-based therapies for wound biofilm infection: Oportunities and challenges. *IEEE Trans. Nanobiosci.* **15**, 294–304 (2016).

17. Bjarnsholt, T. The role of bacterial biofilms in chronic infections. *APMIS* **121**, 1–58 (2013).

18. Jamal, M. et al. Bacterial biofilm and associated infections. *J. Chin. Med. Assoc.* **81**, 7–11 (2018).

19. Benoit, D. & Koo, H. Targeted, triggered drug delivery to tumor and biofilm microenvironments. *Nanomedicine* **11**, 873–879 (2016).

20. Stokes, J. M., Lopatkin, A. J., Lobritz, M. A. & Collins, J. J. Bacterial metabolism and antibiotic efficacy. *Cell Metab.* **30**, 251–259 (2019).

21. Kohanski, M. A. et al. A common mechanism of cellular death induced by bactericidal antibiotics. *Cell* **130**, 797–810 (2007).

22. Allison, K. R., Brynildsen, M. P. & Collins, J. J. Metabolite-enabled eradication of bacterial persisters by aminoglycosides. *Nature* **473**, 216–220 (2011).

23. Davies, D. Understanding biofilm resistance to antibacterial agents. *Nat. Rev. Drug Discovery* **2**, 114–122 (2003).

24. Choi, K. Y. et al. Self-assembled hyaluronic acid nanoparticles for active tumor targeting. *Biomaterials* **31**, 106–114 (2010).

25. Ahmadi, F., Shabrandi, N., Hosseinzadeh, L. & Azizian, H. Two DNA binding modes of a zinc-metronidazole and biological evaluation as a potent anti-cancer agent. *Nucleosides, Nucleotides Nucleic Acids* **38**, 449–480 (2019).

26. Castilho, M., Hewitt, K. & Raniero, L. FT-IR characterization of a theranostic nanoprobe for photodynamic therapy and epidermal growth factor receptor targets. *Sens. Actuators, B* **240**, 903–908 (2017).

27. Kim, H. et al. ROS-responsive activatable photosensitizing agent for imaging and photodynamic therapy of activated macrophages. *Theranostics* **4**, 1–11 (2013).

28. Liu, Y. et al. Eradication of multidrug-resistant Staphylococcal infections by light-activatable micellar nanocarriers in a murine model. *Adv. Funct. Mater.* **27**, 1701974 (2017).

29. Ammons, M. et al. Quantitative NMR metabolite profiling of methicillin-resistant and methicillin-susceptible S*taphylococcus aureus* discriminates between biofilm and planktonic phenotypes. *J. Proteome Res.* **13**, 2973–2985 (2014).

30. Chakravortty, D. et al. Ultrastructural study on the antibacterial activity of artonin E versus streptomycin against S*taphylococcus aureus* strains. *PLoS One* **10**, e0128157 (2015).

31. Lee, A. S. et al. Methicillin-resistant S*taphylococcus aureus*. *Nat. Rev. Dis. Primers* **4**, 18033 (2018).

32. Cederbrant, G., Kahlmeter, G. & Asa, L. Proposed mechanism for metronidazole resistance in Helicobacter pylori. *J. Antimicrob. Chemother.* **29**, 115–120 (1992).

33. Lindmark, D. G. & Mvller, M. Antitrichomonad action, mutagenicity, and reduction of metronidazole and other nitroimidazoles. *Antimicrob. Agents Chemother.* **10**, 476–482 (1976).

34. Kedderis, G. L., Argenbright, L. S. & Miwa, G. T. Mechanism of reductive activation of a 5-nitroimidazole by flavoproteins: Model studies with dithionite. *Arch. Biochem. Biophys.* **262**, 40–48 (1988).

35. Dingsdag, S. A. & Hunter, N. Metronidazole: An update on metabolism, structure-cytotoxicity and resistance mechanisms. *J. Antimicrob. Chemother.* **73**, 265–279 (2018).

36. Tavares, A., Nobre, L. S., Melo, A. & Saraiva, L. M. A novel nitroreductase of S*taphylococcus aureus* with S-nitrosoglutathione reductase activity. *J. Bacteriol.* **191**, 3403–3406 (2009).

37. Löfmark, S., Edlund, C. & Nord, C. Metronidazole is still the drug of choice for treatment of anaerobic infections. *Clin. Infect. Dis.* **50**, 16–23 (2010).

38. Chevalier, A. et al. Mitochondrial nitroreductase activity enables selective imaging and therapeutic targeting. *J. Am. Chem. Soc.* **138**, 12009–12012 (2016).

39. Roldan, M. D., Perez-Reinado, E., Castillo, F. & Moreno-Vivian, C. Reduction of polynitroaromatic compounds: The bacterial nitroreductases. *FEMS Microbiol. Rev.* **32**, 474–500 (2008).

40. Xiu, W. et al. Biofilm microenvironment-responsive nanotheranostics for dual-mode imaging and hypoxia-relief-enhanced photodynamic therapy of bacterial infections. *Research* 2020, 9426453 (2020).

41. Mao, D. et al. Metal-organic-framework-assisted *in vivo* bacterial metabolic labeling and precise antibacterial therapy. *Adv. Mater.* **30**, 1706831 (2018).

42. Chen, Q. et al. *In situ* sprayed bioresponsive immunotherapeutic gel for post-surgical cancer treatment. *Nat. Nanotechnol.* **14**, 89–97 (2019).

43. Xu, J. et al. Hypoxic glioma-derived exosomes promote M2-like macrophage polarization by enhancing autophagy induction. *Cell Death Dis.* **12**, (2021).

44. Mantovani, A. et al. Macrophage plasticity and polarization in tissue repair and remodelling. *J. Pathol.* **229**, 176–185 (2013).

45. Kim, B. et al. Immunogene therapy with fusogenic nanoparticles modulates macrophage response to S*taphylococcus aureus*. *Nat. Commun.* **9**, 1969 (2018).

46. Hart, T., Milner, R. & Cifu, A. Management of a diabetic foot. *JAMA, J. Am. Med. Assoc.* **318**, 1387–1388 (2017).

47. Wu, Y., Cheng, N. & Cheng, C. Biofilms in chronic wounds: Pathogenesis and diagnosis. *Trends Biotechnol.* **37**, 505–517 (2019).

48. Sonderholm, M. et al. The consequences of being in an infectious biofilm: Microenvironmental conditions governing antibiotic tolerance. *Int. J. Mol. Sci.* **18**, 2688–2701 (2017).

49. Wynn, T. A. & Vannella, K. M. Macrophages in tissue repair, regeneration, and fibrosis. *Immunity* **44**, 450–462 (2016).

50. Hussain, M., Hastings, J. & White, P. A chemically defined medium for slime production by coagulase-negative staphylococci. *J. Med. Microbiol.* **34**, 143 (1991).

51. Ouyang, J. et al. *In situ* sprayed NIR-responsive, analgesic black phosphorus-based gel for diabetic ulcer treatment. *Proc. Natl. Acad. Sci.* **117**, 28667-28677 (2020).

Figures
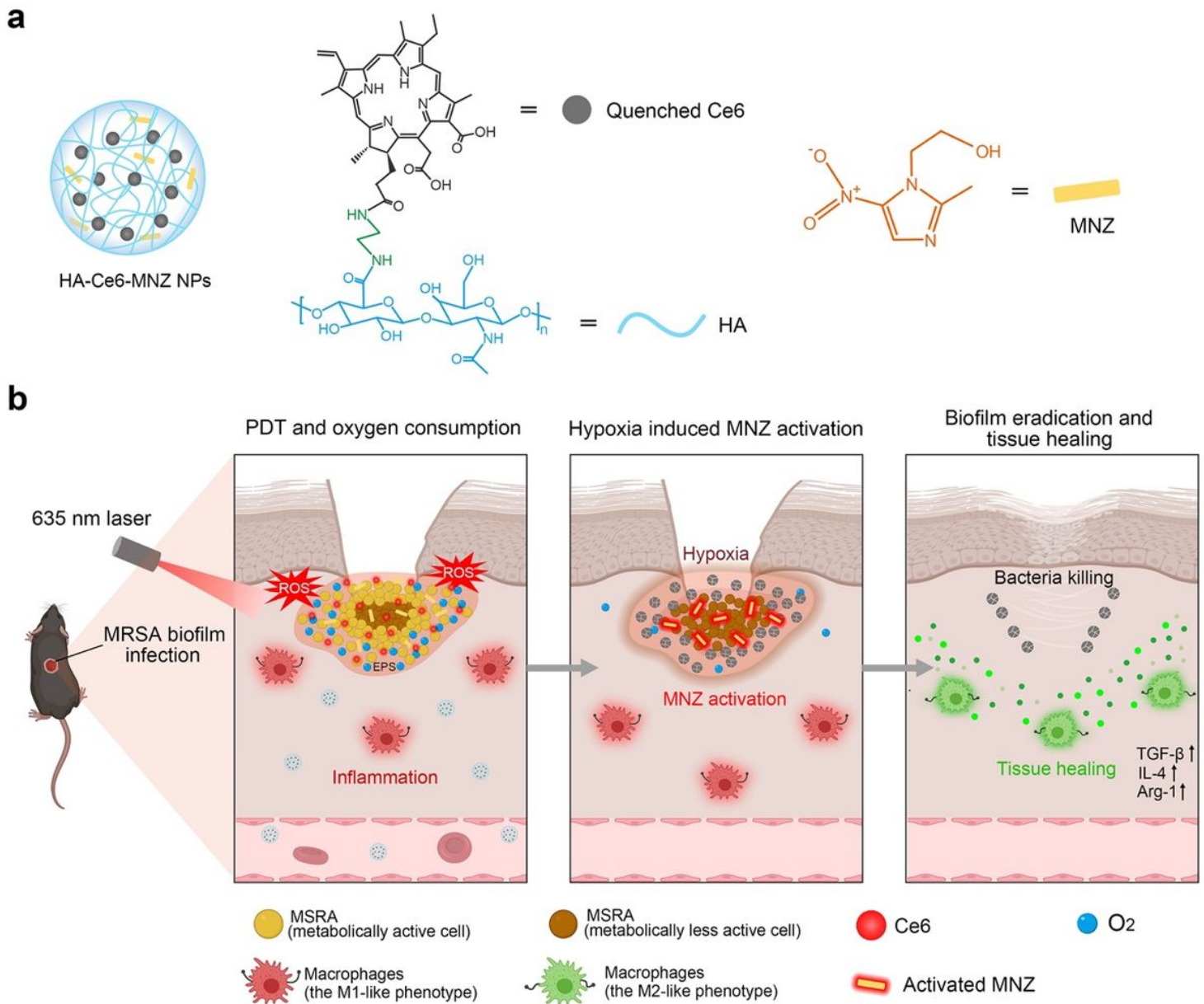
Figure 1

Potentiating hypoxia by PDT for antibiotic activation to combat MRSA biofilm infections. a Schematic illustration of the structure of HA-Ce6-MNZ nanoparticles (HCM NPs). b The therapeutic processes of MRSA biofilms, including the release of Ce6 and MNZ, PDT therapy-potentiated hypoxia, activation of MNZ, elimination of bacterial biofilms, and infected tissue healing.
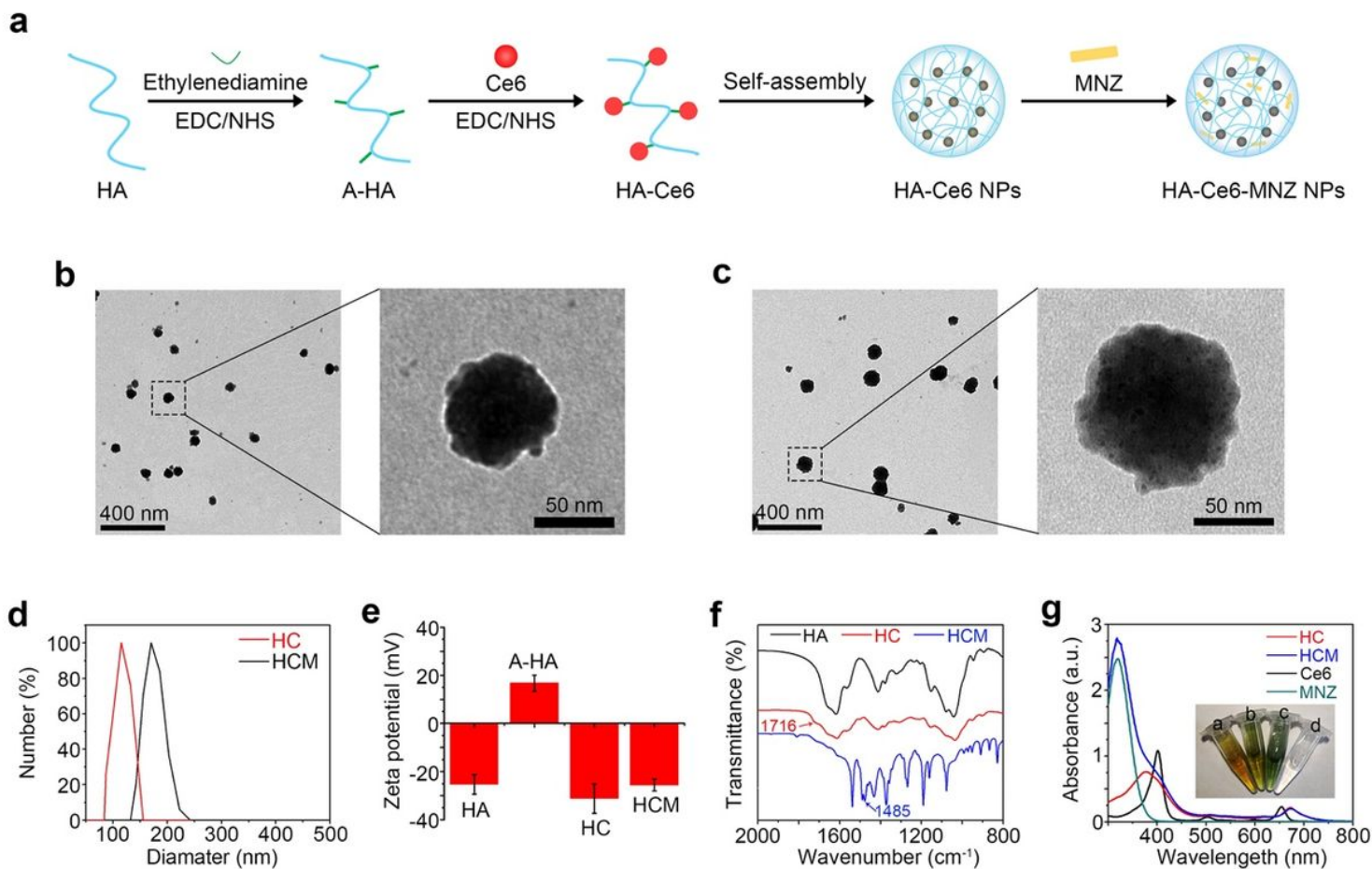
Figure 2

Preparation and characterization of HCM NPs. a Schematic illustration of the preparation of HCM NPs. Transmission electron microscopy (TEM) images of HA-Ce6 NPs (HC NPs) (b) and HCM NPs (c) with low magnification (left) and high magnification (right). d Hydrodynamic sizes of HC NPs and HCM NPs measured by dynamic light scattering (DLS). e Zeta potentials of HA, A-HA, HC NPs, and HCM NPs (n = 3; mean ± SD). f Fourier transformed infrared (FT-IR) spectra of HA, HC NPs, and HCM NPs. g Ultraviolet-visible-near infrared (UV-Vis-NIR) spectra of Ce6, MNZ, HC NPs, and HCM NPs. Inset: photographs of different solutions (a: HC NPs; b: HCM NPs; c: Ce6; d: MNZ).
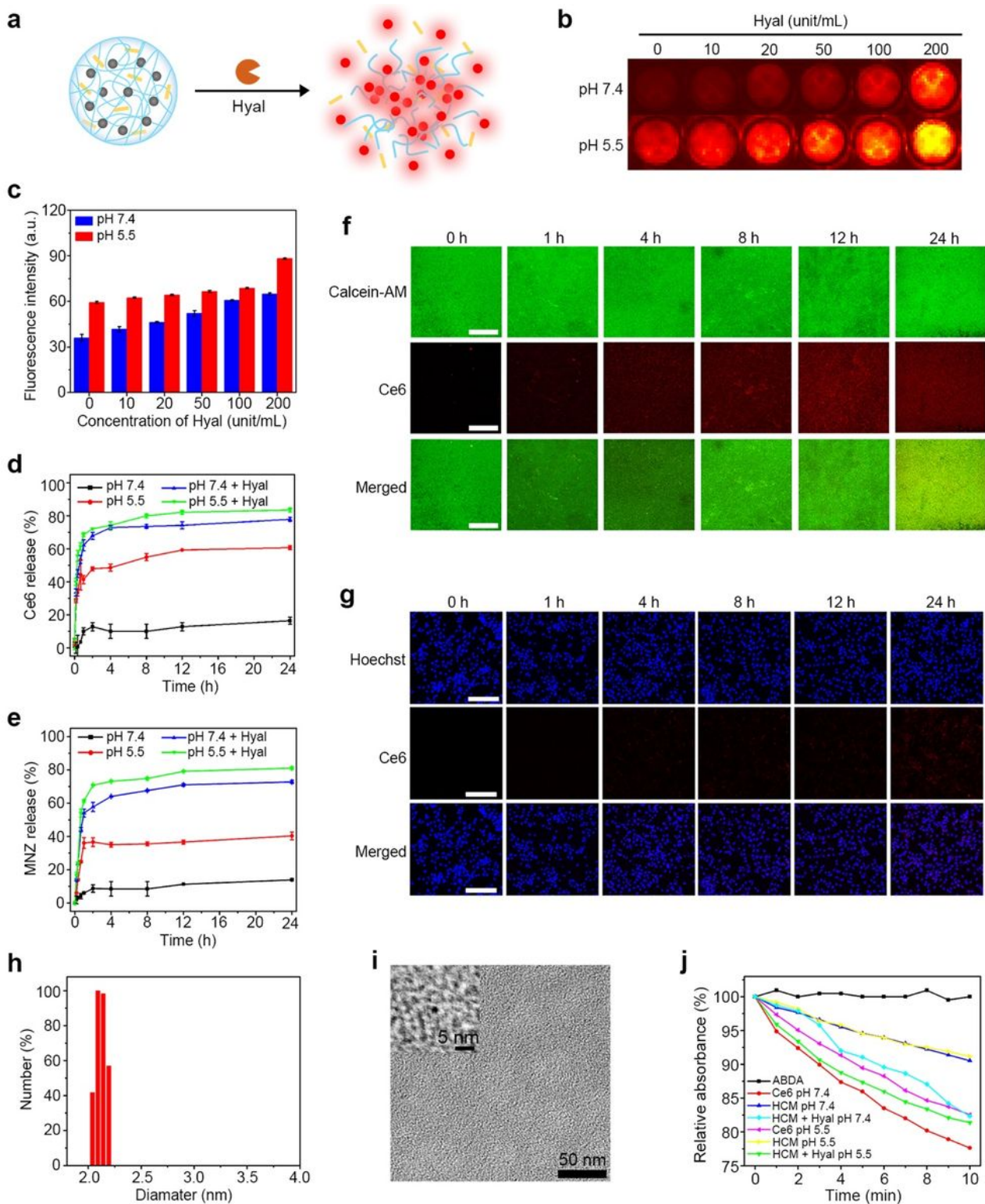
Figure 3

Hyal-responsive drug release of HCM NPs. a Scheme of the decomposition of HCM NPs in presence of Hyal. Fluorescence images (b) and corresponding fluorescence intensity (c) of HCM NPs (Ce6: 40 µg/mL) after incubation with Hyal at different concentrations for 12 h (n = 3; mean ± SD). Release of Ce6 (d) and MNZ (e) from HCM NPs (Ce6: 40 µg/mL; MNZ: 20 µg/mL) under different conditions (n = 3; mean ± SD). Confocal laser scanning microscopy (CLSM) images of MRSA biofilms (f) and SMCs (g) after incubation

with HCM NPs (Ce6: 50 µg/mL; MNZ: 25 µg/mL) for different times. Scale bar is 200 µm. Hydrodynamic size (h) and TEM images (i) of HCM NPs after incubation with Hyal (100 unit/mL) for 24 h. j Relative absorbance of ABDA at 380 nm (OD380) after incubation at various conditions under laser irradiation (635 nm, 20 mW/cm2) for different times.
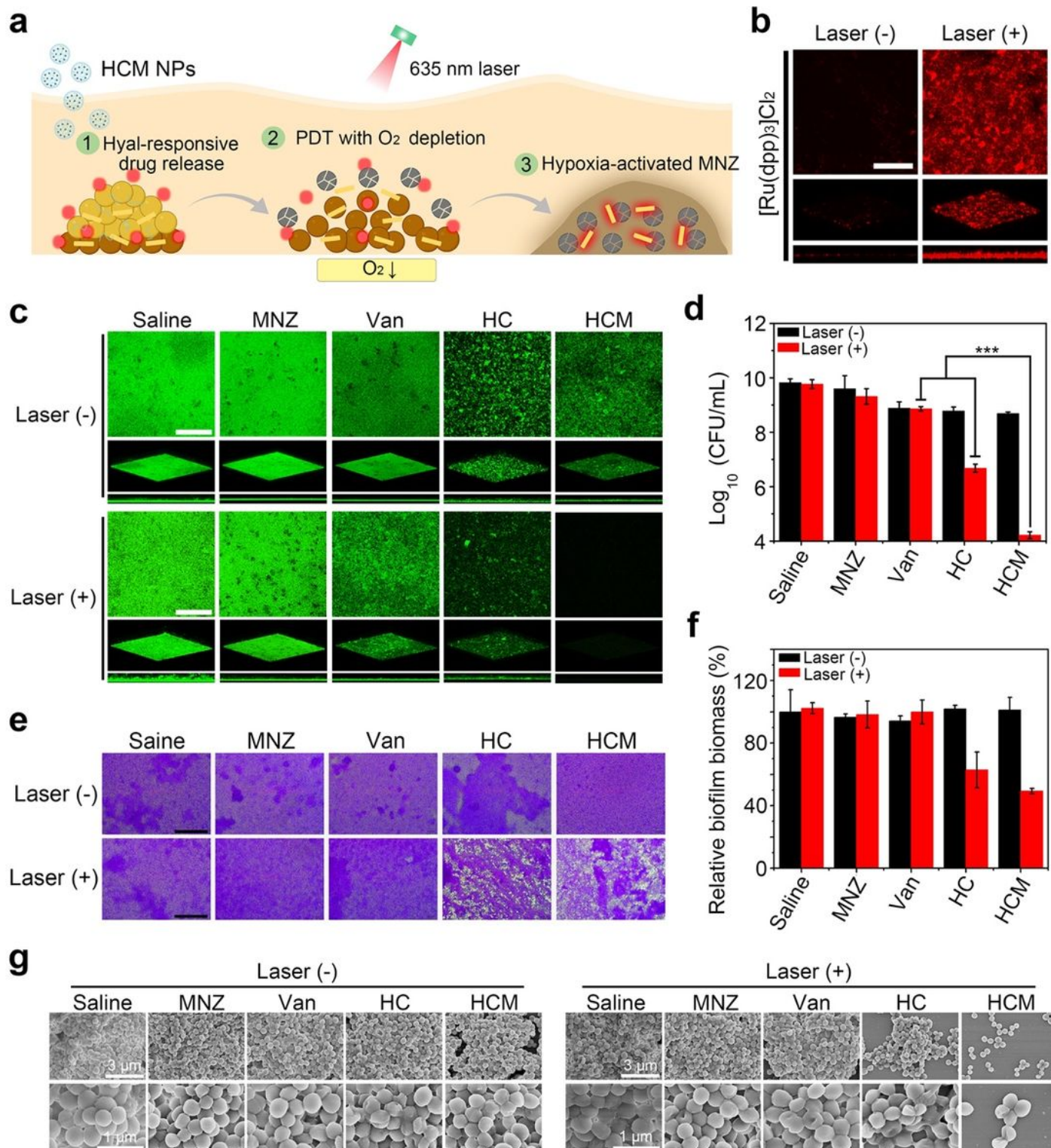

Figure 4

PDT-activated chemotherapy of MRSA biofilms by hypoxia potentiation. a Schematic illustration of the PDT-induced hypoxia and subsequent activation of MNZ for enhanced anti-biofilm treatment by HCM NPs. b 3D CLSM images of $[Ru(dpp)_3]Cl_2$ stained MRSA biofilms with or without PDT (635 nm, 20 mW/cm2, 30 min) by HCM NPs. Scale bar is 200 μm. Size of CLSM images is 630 μm × 630 μm. c 3D CLSM images of MRSA biofilms stained by Calcein-AM (green) after various treatments. Size of CLSM images is 630 μm × 630 μm. Scale bar is 200 μm. d Numbers of viable MRSA within biofilms after various treatments (n = 3; mean ± SD). Statistical significance was calculated via Student's t-test. ***p<0.001. e Micrographs of MRSA biofilms stained by crystal violet after various treatments. Scale bar is 200 μm. f Relative biofilm biomass of MRSA biofilms after various treatments (n = 3; mean ± SD). g Scanning electron microscopy (SEM) images of MRSA biofilms after various treatments.
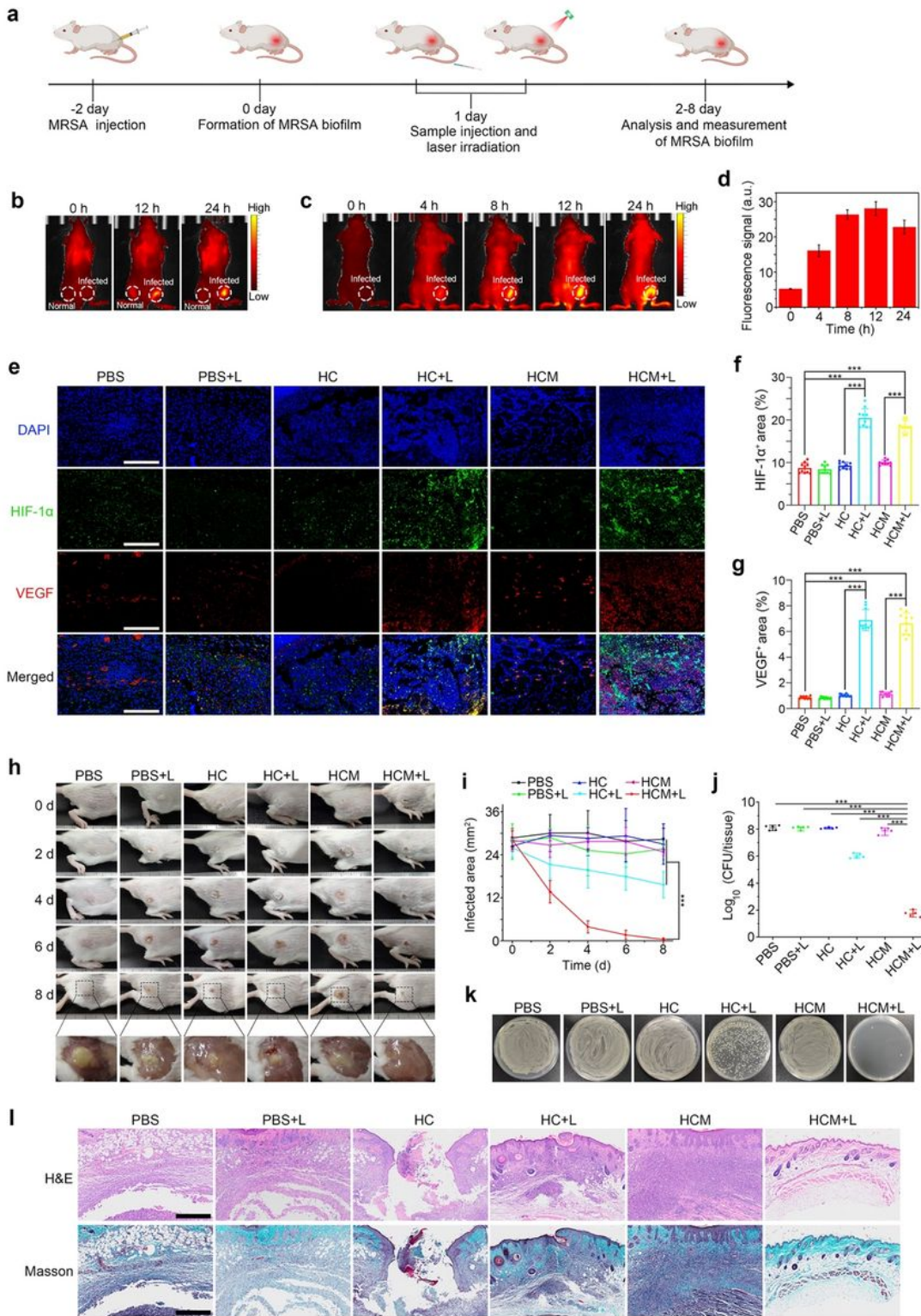
Figure 5

Treatment of subcutaneous MRSA biofilm infected mice by HCM NPs. a Schematic illustration of the experimental procedure for treating MRSA biofilm infected mice. b Fluorescence images of MRSA biofilm infected mice after in situ injection of HCM NPs (Ce6: 100 μg/mL, 50 μL) in normal tissues (left side of thigh) and biofilm infected tissues (right side of thigh), respectively. Fluorescence images of MRSA biofilm infected mice (c) after i.v. injection of HCM NPs (Ce6 = 4 mg/kg; MNZ = 2 mg/kg) and their

average fluorescence signal (d) (n = 3; mean ± SD). e Representative immunofluorescence images of HIF-1α (green) and VEGF (red) in MRSA biofilm infected tissues after various treatments for 4 d. Scale bar is 400 μm. The percentage of HIF-1α+ (f) and VEGF+ (g) area in various treatment groups calculated from the immunofluorescence images (n = 10). Photographs of the infected tissues (h) and infected area (i) of the mice after various treatments (n = 5; mean ± SD). j Quantification of viable bacteria inside biofilm infected tissues at 8 d post-treatment (n = 5; mean ± SD). k Photographs of MRSA colonies from infected tissues at 8 d post-treatment. l H&E and Masson's trichrome stained slices of the infected tissues from mice at 8th d post-treatment. Scale bar is 500 μm. Statistical significance was calculated via Student's t-test. ***$p < 0.001$.
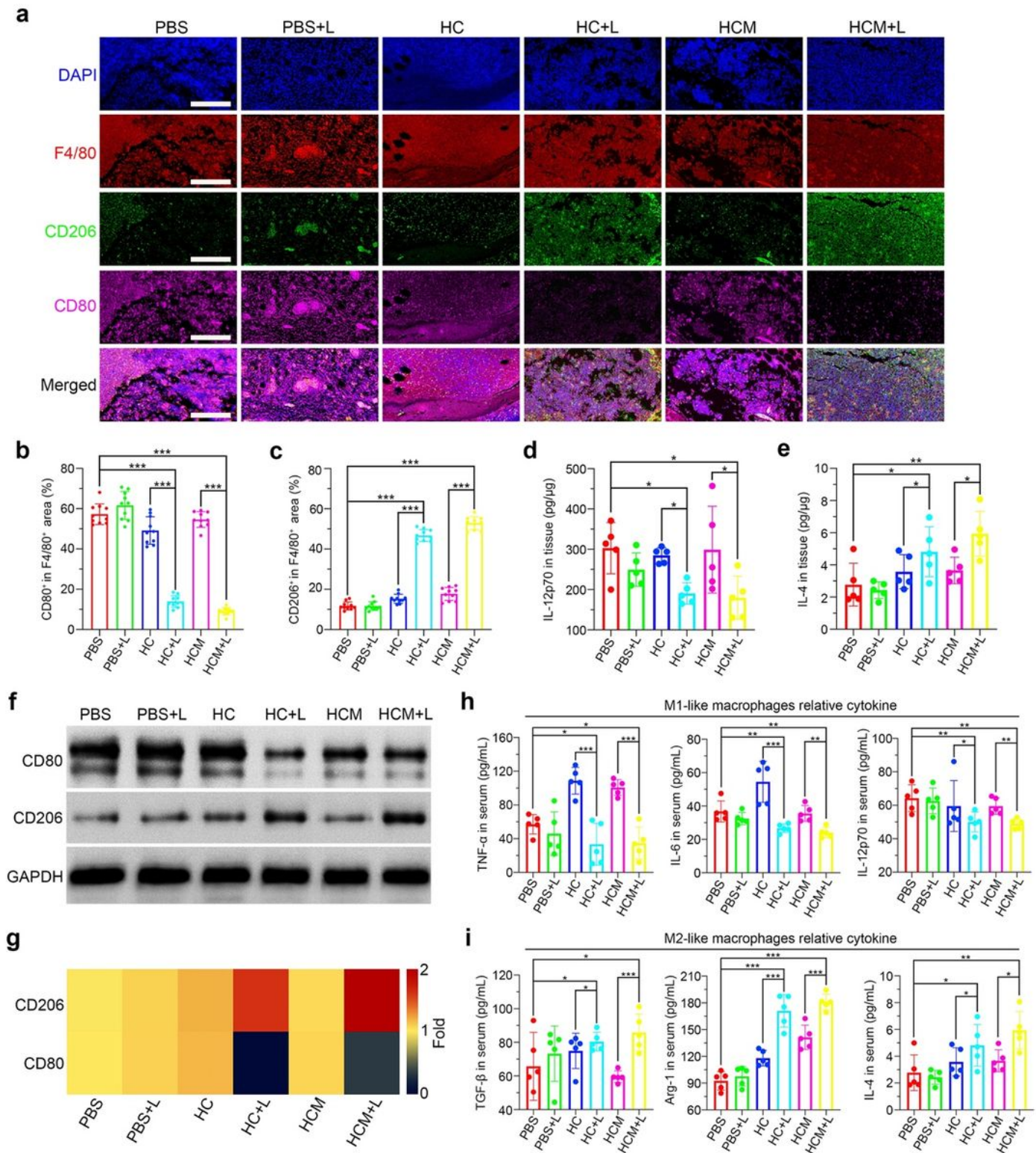
Figure 6

Macrophage polarization of MRSA biofilm infected mice after PDT-activated chemotherapy. a Immunofluorescence images of F4/80 (red), CD206 (green), and CD80 (violet) in the infected tissues after treatment. Scale bar is 400 μm. Percentage of CD80+ (b) and CD206+ (c) area to total F4/80+ area calculated from the immunofluorescence images (n = 10). Secretion level of IL-12p70 (d) and IL-4 (e) in the infected tissues after treatment (n = 5). f Expression level of CD80 and CD206 in the infected tissues

determined by western blotting after treatment. g Heat map of the relative expression of CD80 and CD206 in the infected tissues compared to the PBS group calculated from western blotting results. Secretion level of M1 macrophage-relative cytokines (h) and M2 macrophage-relative cytokines (i) in the serums isolated from mice after treatment (n = 5). Statistical significance was calculated via Student's t-test. *$p<0.05$, **$p<0.01$, ***$p<0.001$.
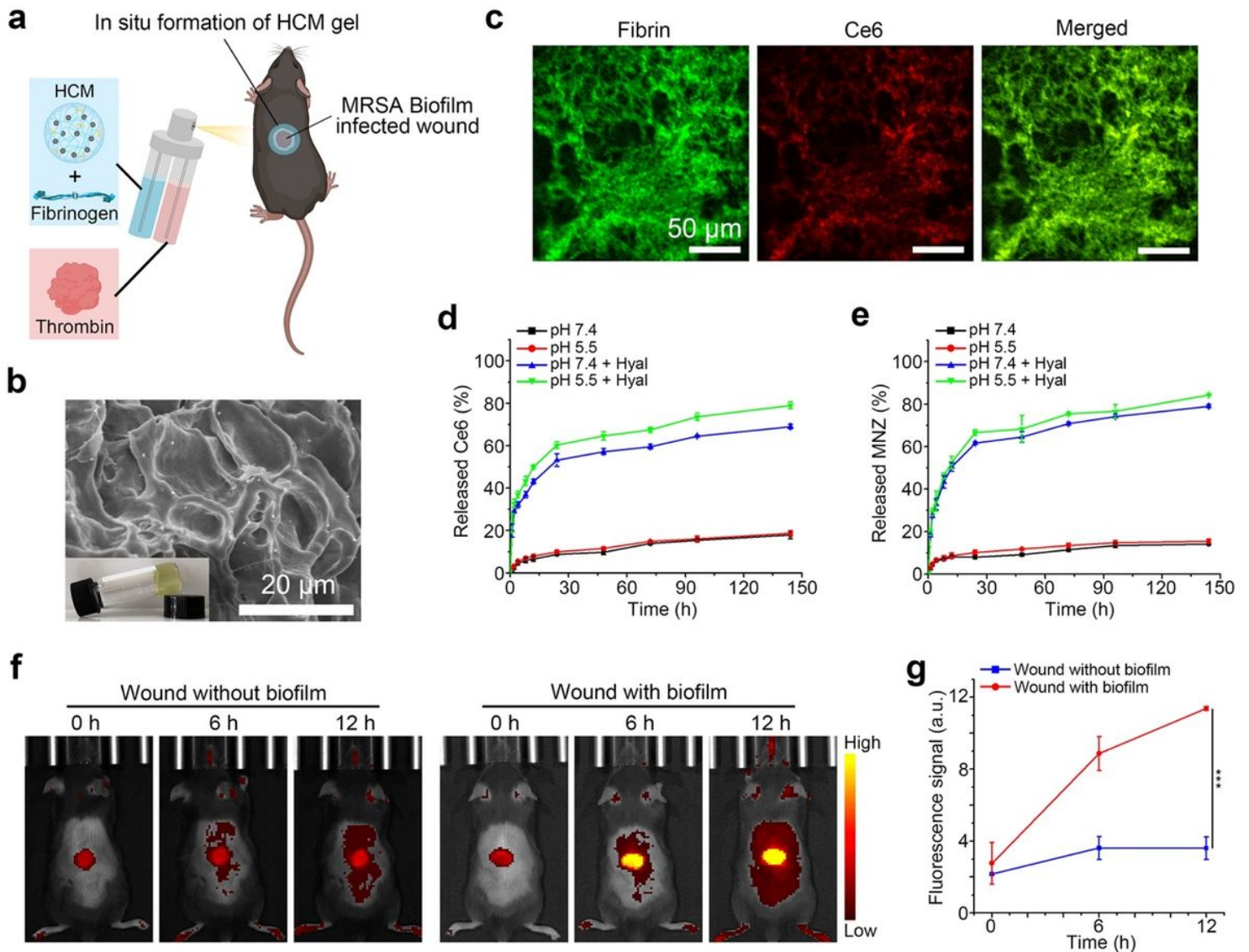

Figure 7

Preparation and characterization of the HCM gel. a Schematic illustration of the HCM gel in situ formed on bacterial biofilm infected wounds. b SEM image of the HCM gel. Inset: photograph of HCM gel. c CLSM images of the HCM gel, in which the fibrinogen was labeled with fluorescein isothiocyanate (FITC, green). Cumulative release profile of Ce6 (d) and MNZ (e) from the HCM gel incubated with or without Hyal under different pH conditions (n = 3; mean ± SD). Fluorescence images (f) and fluorescence intensity (g) of normal wounds and wounds with MRSA biofilm infection in diabetic mice after being treated by HCM gel at different time points (n = 3; mean ± SD). Statistical significance was calculated via Student's t-test. ***$p<0.001$.
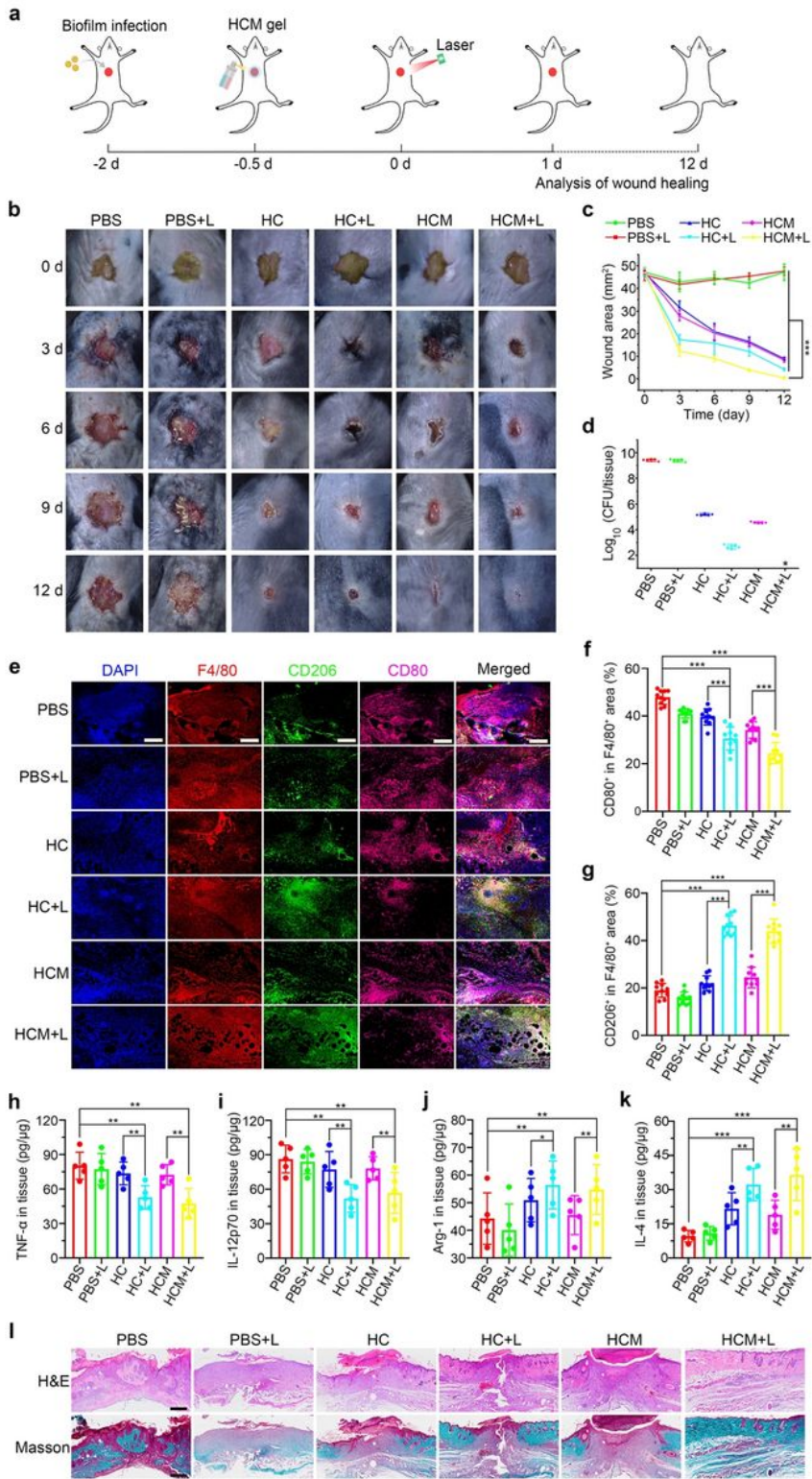
Figure 8

Treatment of MRSA biofilm infected wounds in diabetic mice by HCM gel. a Schematic illustration of the experimental procedure. Photographs (b) and wound area (c) of the infected wounds after treatment (n = 5; mean ± SD). d Colony numbers of bacteria in infected wounds at 12 d post-treatment (n = 5). e Immunofluorescence images of F4/80 (red), CD206 (green), and CD80 (violet) in infected wounds at 4th d post-treatment. Scale bar is 200 μm. Percentage of CD80+ (f) and CD206+ (g) area in F4/80+ area

calculated from immunofluorescence images (n = 10). Secretion level of TNF-α (h), IL-12p70 (i), Arg-1 (j), and IL-4 (k) in infected tissues at 4 d post-treatment (n = 5). l H&E and Masson's trichrome- stained images of infected tissues at 12 d post-treatment. Scale bar is 500 μm. Statistical significance was calculated via Student's t-test. *p<0.05, **p<0.01, ***p<0.001.

Supplementary Files

This is a list of supplementary files associated with this preprint. Click to download.

- SupplementaryMaterialsNatureCommunicationsF.docx